ACS Catalysis

pubs.acs.org/acscatalysis

Research Article

Cobalt-Catalyzed Hydrogenation Reactions Enabled by Ligand-Based Storage of Dihydrogen

Sophie W. Anferov, Alexander S. Filatov, and John S. Anderson*

Cite This: *ACS Catal.* 2022, 12, 9933–9943

Read Online

ACCESS | Metrics & More | Article Recommendations | Supporting Information

ABSTRACT: The use of supporting ligands that can store either protons or electrons has emerged as a powerful strategy in catalysis. While these strategies are potent individually, natural systems mediate remarkable transformations by combining the storage of both protons and electrons in the secondary coordination sphere. As such, there has been recent interest in using this strategy to enable fundamentally different transformations. Furthermore, outsourcing H-atom or hydrogen storage to ancillary ligands can also enable alternative mechanistic pathways and thereby selectivity. Here, we describe the application of this strategy to facilitate radical reactivity in Co-based hydrogenation catalysis. Metalation of previously reported dihydrazonopyrrole ligands with Co results in paramagnetic complexes, which are best described as having Co(II) oxidation states. These complexes catalytically hydrogenate olefins with low catalyst loadings under mild conditions (1 atm H_2, 23 °C). Mechanistic, spectroscopic, and computational investigations indicate that this system goes through a radical hydrogen-atom transfer (HAT) type pathway that is distinct from classic organometallic mechanisms and is supported by the ability of the ligand to store H_2. These results show how ancillary ligands can facilitate efficient catalysis, and furthermore how classic organometallic mechanisms for catalysis can be altered by the secondary coordination sphere.

Ligand Based H_2 Storage for Olefin Hydrogenation

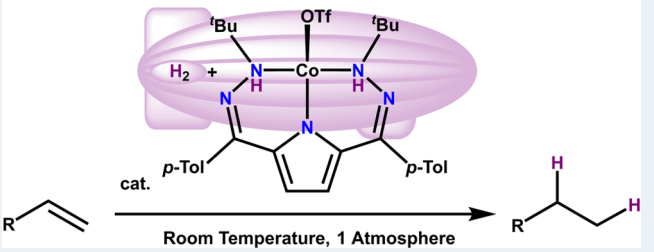

KEYWORDS: *catalysis, redox-active, cobalt, hydrogenation, hydrogen*

INTRODUCTION

The efficient shuttling of protons and electrons is key for many chemical transformations. Metal centers are often employed to facilitate this reactivity, but multi-proton/electron transformations remain challenging, particularly with abundant first-row transition metals with predominant one-electron reactivity.[1] Natural systems have evolved to optimize the use of first-row metals by leveraging a secondary coordination sphere tailored to the needs of a given reaction.[2] Given that the number of protons and electrons stored in the secondary coordination sphere is, in principle, only limited by ligand design, this strategy also opens the door for challenging reactions requiring the transfer of many proton and electron equivalents.

Common secondary sphere motifs utilized in synthetic systems include hydrogen bonding ligands,[3] proton-shuttling functionalities,[4] and redox-active sites that enable electron storage and transfer.[5] Significant effort over the past few decades has illustrated the value of these strategies in facilitating or altering reactivity patterns, but examples where both protons and electrons can be stored on ancillary ligands are comparatively less common. There are several well-defined systems that store H-atom equivalents,[6] and examples of the storage of a full equivalent of dihydrogen in a ligand backbone are even more rare.[7,8] Despite their scarcity, such ligand scaffolds are promising candidates to efficiently facilitate challenging multi-proton/electron transfers in catalysis.

Our laboratory has been interested in first-row transition metal complexes ligated by dihydrazonopyrrole (DHP) ligands. These complexes can reversibly transfer dihydrogen stored on the ligand framework, which enables the catalytic hydrogenation of benzoquinone in a Ni-based system.[9,10] Related Fe complexes are also able to transfer H-atoms to O_2 to generate hydroperoxo intermediates and ultimately H_2O_2 using ligand-derived H-atom equivalents.[11] We rationalized that striking a balance between redox and spin-state flexibility, as present with Fe complexes, and more classic organometallic metals, such as Ni, might be advantageous for new catalytic transformations.[10,11]

In this context, Co features prominently among first-row transition metals in hydrogenation catalysis. Unlike Rh and Ir,

Received: May 25, 2022
Revised: July 18, 2022
Published: August 1, 2022

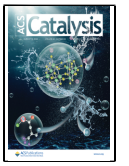

https://doi.org/10.1021/acscatal.2c02467
ACS Catal. 2022, 12, 9933–9943

Co does not necessarily proceed through classical two-electron transformations and, as with other first-row transition metals, exhibits a propensity for single-electron steps and varied spin states.[12−14] These alternative trends can also be leveraged to obtain altered reactivity. For instance, recent reports have illustrated how Co complexes with ligands that can store protons or electrons can efficiently mediate catalytic hydrogenations, with some examples exhibiting alternative mechanistic pathways in the presence of light (Figure 1).[12,14]

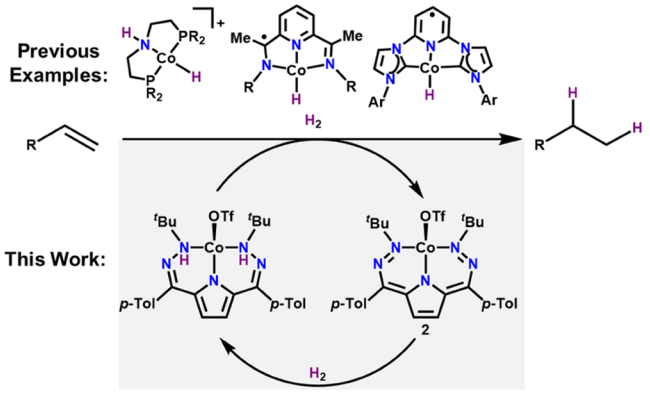

Figure 1. Existing Co-based hydrogenation catalysts or active species[12c,e,14a,b,d,e,15a] and the current system highlighting ligand-based H_2 storage.

Given this precedent for Co in hydrogenation chemistry and the opportunities that it presents as a first-row metal, we were interested in examining the interplay between Co centers and DHP ligands in H-transfer chemistry. Specifically, we sought to investigate whether Co DHP complexes were viable hydrogenation catalysts and, if so, whether the DHP ligand would enable alternative mechanisms to more canonical organometallic pathways.[12−14] Here, we present a series of ^{tBu,Tol}DHP Co catalysts that mediate olefin hydrogenation via a ligand-assisted hydrogenation pathway. Catalysis occurs efficiently under mild conditions, comparable with the best Co hydrogenation catalysts currently known.[14e,15] Spectroscopic, computational, and mechanistic investigations demonstrate that catalysis proceeds via a radical H-atom transfer mechanism supported by the ^{tBu,Tol}DHP ligand. These results illustrate how cooperativity between Co centers and ligands which can store H-atom or H_2 equivalents enables efficient catalysis with novel mechanistic paradigms.

RESULTS AND DISCUSSION

Synthesis and Characterization of 1. Deprotonation of ^{tBu,Tol}DHP·2HCl[9c] with 2.8 equiv of KHMDS followed by the rapid addition of a $CoCl_2$ suspension in THF and a single equivalent of 1-hexene (acting as a H_2 acceptor) provides [^{tBu,Tol}DHP]CoCl (**1**) as a magenta-purple solid in 75% yield (Scheme 1). We note this reaction still provides **1** as the major product in the absence of 1-hexene as a H_2 acceptor, albeit in lower yields. Dark purple crystals suitable for single-crystal X-ray diffraction (SXRD) reveal a four-coordinate Co complex. The geometry of **1** can be quantified with τ_4 and τ_4' values of 0.473 and 0.363, respectively, suggesting a see-saw complex with some tetrahedral character (Figure 2 and Table 1).[16]

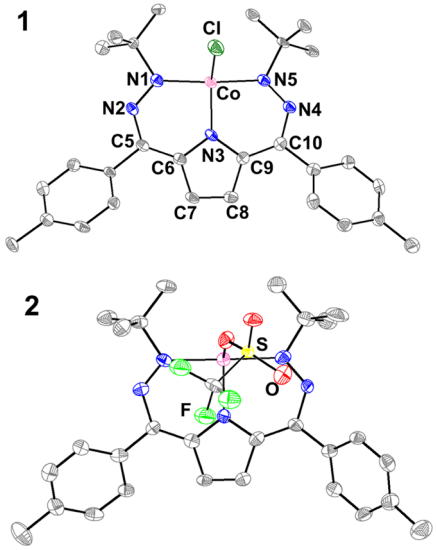

Figure 2. SXRD Structures (from left to right) of **1** and **2**. All displacement ellipsoids shown at 50%, and hydrogens omitted for clarity.

Complex **1** is paramagnetic with an $S = 1/2$ solution spin state as determined by Evans' method. This suggests either a low-spin Co(II) center with a DHP$^-$ ligand or a Co(III) center with a DHP$^{2-\bullet}$ ligand radical. We note that there are several examples of low-spin Co(II) complexes in similar geometries,

Scheme 1. Synthesis of ^{tBu,Tol}DHP Complexes of Co and Hydrogenation Reactivity

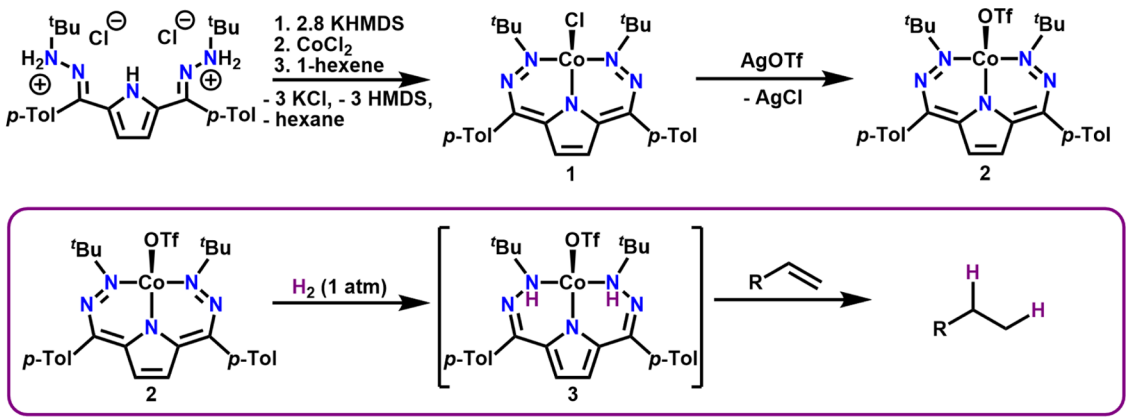

https://doi.org/10.1021/acscatal.2c02467
ACS Catal. 2022, 12, 9933−9943

Table 1. Selected Bond Lengths (Å) and Angles (°) of 1, 2, and Related Ni Complexes

	1	2[a]	[DHP$^{2-\bullet}$]NiL[9a]	[DHP^{-}]NiL^{+}[9a]
M-N1/M-N5	1.891(5)	1.994(8)	1.866(2)	1.864(2)
	1.883(4)	2.000(8)	1.863(2)	1.860(2)
M-N3	1.861(4)	1.916(8)	1.872(2)	1.869(2)
N1-N2/N4-N5	1.303(6)	1.27 (1)	1.342(2)	1.302(2)
	1.288(6)	1.25(1)	1.337(3)	1.314(2)
M-X(Cl/O/P)	2.198(2)	2.168(7)	2.2319(7)	2.2630(7)
M-X(N/O)		2.126(7)		
N2-C5/N4-C10	1.343(7)	1.37(1)	1.319(3)	1.348(2)
	1.338(7)	1.39(1)	1.322(2)	1.342(3)
C5-C6/C9-C10	1.383(8)	1.38 (1)	1.417(3)	1.388(3)
	1.388(8)	1.38(1)	1.425(3)	1.393(3)
C6-C7/C8-C9	1.434(8)	1.43(1)	1.413(3)	1.444(3)
	1.433(8)	1.45(1)	1.421(3)	1.452(3)
C7-C8	1.351(8)	1.31(1)	1.371 (3)	1.343 (3)
N1-M-N5	164.5(2)	178.1(3)	163.59(8)	161.85(7)
N3-M-X	129.1(2)	113.2(3)	145.30(6)	142.64(5)
		105.1(3)		

[a]Crystallizes as a polymeric chain; monomer shown. L = PMe_3 as described in the text.

including a number of imino-pyridine ligated Co(II) complexes as well as Co porphyrin and corrin species.[17,18,21]

The structure of **1** provides the opportunity to examine limiting electronic structures. We have found that the electronic structure of the DHP ligand results in changes to specific bonds in the scaffold in a diagnostic manner, namely, the N1-N2/N4-N5, C5-C6/C9-C10, and C7-C8 distances.[9,10] Comparison of these distances between **1** and the previously reported four-coordinate Ni complexes [^{Ph,Tol}DHP]NiPMe$_3^{n+}$ (n = 0 and 1) suggests that the DHP ligand in **1** is best considered as a closed-shell monoanionic DHP^{-} unit, thereby implying a Co(II) oxidation state.[9a] However, this interpretation is convoluted by the differing metal centers and ligand sets in this comparison.

Complex **1** displays four distinct redox waves in its cyclic voltammogram (CV, Figure S19). This electrochemical data shows that the ^{tBu,Tol}DHP scaffold supports unusually rich redox flexibility in this system. Despite this, complex **1** does not exhibit discernible reactivity with H_2. We hypothesized that the exchange of chloride for a less-coordinating anion could promote reactivity with H_2 and potentially catalysis.

Synthesis and Characterization of 2. Complex **1** reacts with AgOTf in a mixture of benzene/acetonitrile to produce [^{tBu,Tol}DHP]CoOTf (**2**) as a maroon solid (Scheme 1). Similar to **1**, complex **2** is also paramagnetic with an S = 1/2 spin state as determined by Evans' method. SXRD analysis on the very dark crystals of **2** reveals a Co center that is five-coordinate due to the formation of a polymeric chain from bridging OTf^{-} ligands in the solid state. The τ_5 value for this complex is 0.605, putting it closer to trigonal bipyramidal than square pyramidal (at 1 and 0, respectively).[19] Examination of the monomeric repeat unit of **2** reveals that the bond lengths within the DHP ligand undergo changes from those in **1**, which suggests a more distinctively oxidized DHP^{-} ligand, and hence also a Co(II) oxidation state assignment (Figure 1 and Table 1). The CV of **2** is qualitatively similar to that of **1**, albeit less reversible overall, likely due to enhanced lability of the OTf^{-} counteranion (Figure S20).

We then acquired electron paramagnetic resonance (EPR) spectroscopy to better understand the relative electronic structures of complexes **1** and **2**. The EPR of **1** is rhombic, with g-values of 2.02, 2.10, and 2.58 (Figures S21 and S22). EPR spectra of organic radicals are typically more isotropic and with all g-values near g = 2.0, suggesting that a Co(II) electronic structure may be appropriate.[20] Indeed, literature examples where a five- or six-coordinate Co(III) center is bound to a ligand radical as well as previous examples with DHP radical ligands, namely, [^{tBu,Tol}DHP$^{2-\bullet}$]Ni and [^{Ph,Tol}DHP$^{2-\bullet}$]Ni, all have smaller g-anisotropy than that of **1**, further supporting a [DHP^{-}]Co(II) resonance structure.[9a,21,9c] While the greater g-anisotropy of **1** is different from low spin, square-planar cobalt complexes,[22] it is distinctly similar to related tetrahedral or see-saw complexes.[23] The best simulation we have obtained uses hyperfine coupling (MHz) to both ^{59}Co (A_{xx} = 57.6, A_{yy} = 62.4, A_{zz} = 58.8) and ^{14}N (A_{xx} = 35.4, A_{yy} = 44.7, A_{zz} = 10.7), although we note that the complicated pattern means that alternative spin systems, for instance, those with coupling to more than one ^{14}N nucleus, may also provide satisfactory fits. While the g-anisotropy and ^{59}Co hyperfine constants support a Co(II) oxidation state, the large ^{14}N hyperfine suggests that there is still significant spin on the DHP ligand. Density Functional Theory (DFT) calculations with the B3P functional support this notion. While the majority of the spin density is localized on Co, a significant fraction (30%) is present on the DHP ligand (Figure S35).

The EPR spectrum of **2** is similarly rhombic to that of **1** with g-values of 2.01, 2.11, and 2.61, and our best simulation similarly features coupling (MHz) to both ^{59}Co (A_{xx} = 56.5, A_{yy} = 89.0, A_{zz} = 75.6) and ^{14}N (A_{xx} = 12.1, A_{yy} = 5.9, A_{zz} = 11.2) (Figure 3). As with **1**, this data suggests that the best description of **2** is as a low-spin Co(II) center with an oxidized monoanionic ^{tBu,Tol}DHP ligand. Consistent with the structural data above, the relative g-anisotropies and hyperfine constants between **1** and **2** both support that **2** is closer to a "pure" Co(II) resonance structure, although we note that DFT calculations still support some radical character on the DHP ligand (20%, Figure S37).

As a final probe of electronic structure, we obtained Co K-edge X-ray absorption spectroscopy (XAS) data on both **1** and **2**. The pre-edge feature for **1** is only slightly shifted to higher energy from **2** by 0.4 eV (from 7709.3 to 7709.7 eV), which is

https://doi.org/10.1021/acscatal.2c02467
ACS Catal. 2022, 12, 9933−9943

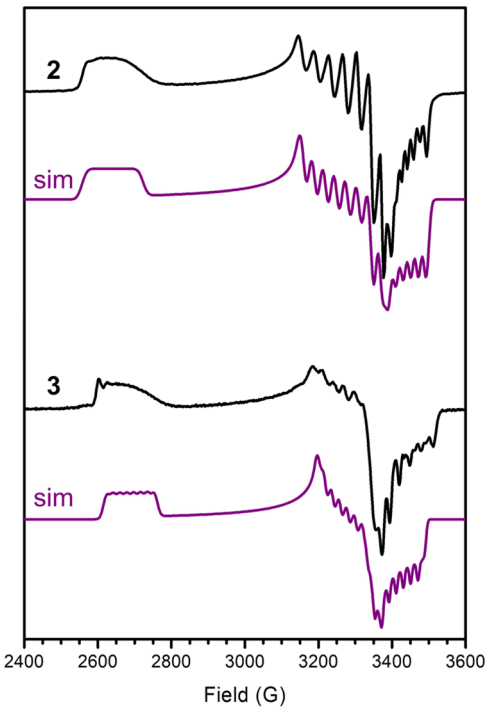

Figure 3. Perpendicular mode X-band EPR spectrum from top to bottom of 15 mM solutions of **2** and **3** at 15.9 K in toluene and 20 K in toluene, respectively. Simulation shown in black lines for each. Simulation parameters for **2**: g = 2.01, 2.11, 2.61; Co-A = +56.5, +89.0, +75.6 MHz; N-A = +12.1, +5.9, +11.2 MHz. **3**: g = 2.02, 2.10, 2.56; Co-A = +54.8, +61.0, +66.8 MHz, N-A = +23.1, +24.5, −14.1 MHz. Experimental conditions: microwave frequency 9.6304 GHz, microwave power 0.2 mW. The full and simulated spectra are shown in the SI (Figures S21−S27 and Table S1).

at the experimental resolution, and the K-edges for these two complexes are also quite similar (Figures S28−S29).[24] This data again supports similar electronic structures between **1** and **2** and are consistent with other Co(II) complexes.[14b25] Thus, while the electronic structures of these complexes, particularly **1**, are highly covalent with reasonably invoked DHP non-innocence, the best limiting resonance contributor is [DHP^{-}]$^{-}$Co(II).

Generation and Characterization of 3. While **1** shows no reactivity with H_2, addition of H_2 to cold solutions of **2** results in a new magenta product (**3**) (Scheme 1). Complex **3** forms very slowly, taking over 48 h for complete conversion at −25 °C, and is unstable at and above 0 °C. The use of D_2 results in significantly slower conversion but still allows for the formation of enough **3-D$_2$** for IR characterization (Figure 4). Though **3** is unstable to higher temperatures, it is stable to vacuum once formed.

The ^{1}H NMR spectrum of **3** is paramagnetic and broad (Figure S2). This is consistent with 2 e$^-$ reactivity with H_2, and we have tentatively assigned **3** as the hydrogenated product, [$^{t\text{Bu,Tol}}$DHP-H$_2$]CoOTf, analogously to the reactivity observed with a related Ni system.[10] The EPR signal of **3** at 20 K further supports this assignment, with an observed major S = 1/2 signal along with a small amount (<10%) of unconverted **2** (Figure 3, bottom). Fitting of the major species reveals parameters that are quite similar to **1** and **2**, with g-values of 2.02, 2.10, and 2.56 and hyperfine coupling (MHz) to both ^{59}Co (A_{xx} = 54.8, A_{yy} = 61.0, A_{zz} = 66.8) and ^{14}N (A_{xx} = 23.1.645, A_{yy} = 24.5, A_{zz} = −14.1). Importantly, the EPR spectrum of **3** is less consistent with a Co−H assignment; inclusion of any significant hyperfine coupling to ^{1}H notably worsens the fit. The Co K-edge XAS data for **3** has the same 0.4 eV shift to lower energy versus **1**, which again supports a very similar Co oxidation state across these three compounds (Figures S30 and S31).

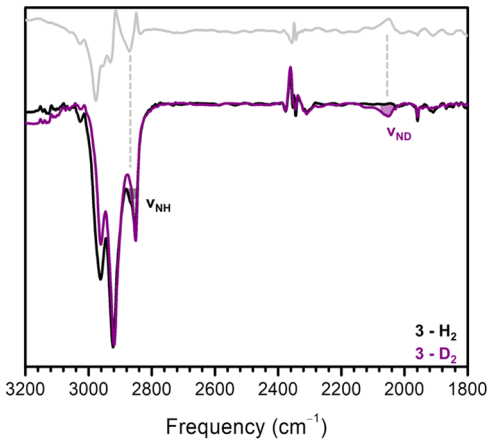

Figure 4. Thin-Film IR spectrum of **3** and **3-D$_2$** with difference spectrum in the inset.

We then turned to verifying the presence and investigating the localization of the added protons from hydrogenation. Hydrogenated and deuterated samples were prepared at −25 °C in minimal toluene over 48 or 72 h under ∼3 atm of H_2 or D_2, respectively. These samples were kept cold throughout drying and sample preparation. Both mineral oil and thin-film IR samples reproducibly show a clear N−D stretch in the deuterated samples around 2065 cm^{-1} (Figure 4, Table S63 and eq S1). The corresponding isotopically shifted feature is not immediately apparent in the spectrum of proteo-**3** due to convolution with C−H stretches, but a subtraction spectrum does indicate the presence of a feature underneath these other stretches at ∼2870 cm^{-1} that is consistent with a N−H functionality and which closely corresponds to the DFT-predicted N−H stretch of 2922 cm^{-1} (Table S63). This result confirms that the reactivity with H_2 involves the formation of N−H's on the $^{t\text{Bu,Tol}}$DHP ligand. As a final verification of the assigned structure of **3**, time-dependent DFT (TD-DFT) calculations were performed to compare the predicted and experimental UV−visible (UV−vis) spectra of **3**. The theoretical UV−vis spectrum of **3** using the PBE0 functional on the previously optimized geometry matches well with the experimental spectrum, further supporting our assignment (Figure S87).

Hydrogenation Catalysis. Given the reactivity observed with dihydrogen to form **3**, we wanted to test if **2** could be used as a hydrogenation catalyst. Given its use in the synthesis of **1**, we initially chose 1-hexene as a test substrate under mild conditions (1 atm of H_2, 23 °C). We observed 79(6)% conversion to hexane with 1% catalyst loading of **2** under these conditions, and thus we proceeded to investigate the scope of this reaction with other olefins (Table 2). Terminal mono-substituted olefins are all efficiently hydrogenated, even with comparatively large substrates; 3,3-dimethylbutene is hydrogenated in 71(2)% yield. Alkynes can also be reduced; hydrogenation of 1-hexyne with **2** provides hexane with 69(1)% yield and only 6(3)% of the singly hydrogenated

https://doi.org/10.1021/acscatal.2c02467
ACS Catal. 2022, 12, 9933−9943

Table 2. Hydrogenation Substrate Scope with 2

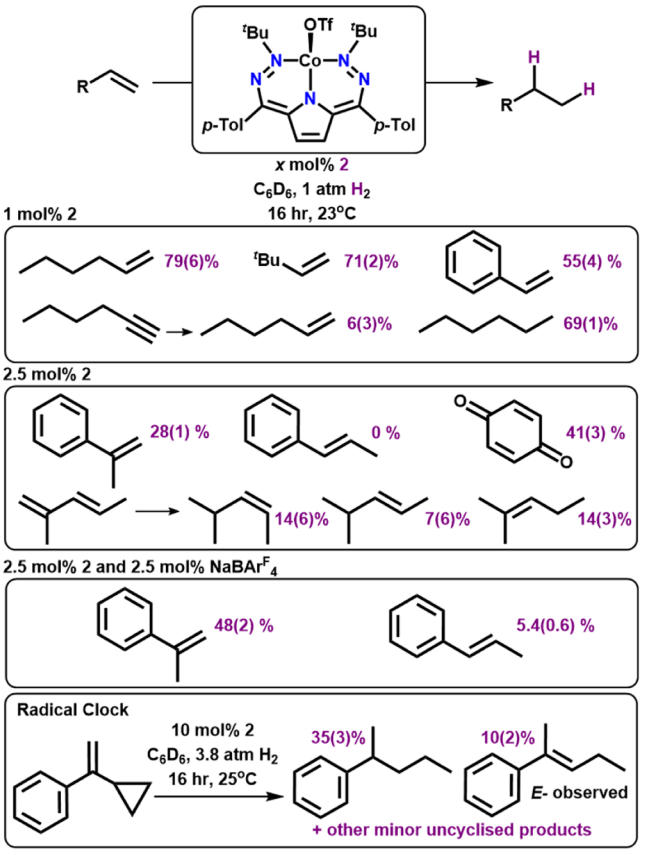

product 1-hexene. A more moderate yield of 55(4)% is obtained with styrene.

Significantly attenuated yields are observed with more sterically encumbering substrates, such as α-methyl styrene, which is hydrogenated in only 28(1)% yield, even with a higher 2.5% catalyst loading. This suggests that steric limitations play a major role in catalysis by **2**, which is perhaps unsurprising given the large *t*-Bu substituents on the DHP ligand. Reactivity is shut down completely with β-methyl styrene even at 2.5% catalyst loadings. Based on mechanistic DFT calculations (see below), we decided to investigate whether OTf^--abstracting reagents might enable higher conversions with these sterically encumbering substrates. In situ addition of $NaBAr_4^F$ (BAr_4^F = tetrakis[3,5-bis(trifluoromethyl)phenyl]borate) as an OTf^- abstractor to the catalytic mixture approximately doubles the yield of cumene from α-methyl styrene to 48(2)% and furthermore enables detectable hydrogenation yields (~5%) for β-methyl styrene. Conversely, the addition of LiOTf to catalytic reactions with α-methyl styrene lowers the yield to 5.8%. These results suggest that the dissociation of triflate is likely important during catalysis and is consistent with DFT calculations that support lower energy pathways for the cationic fragment $[(^{tBu,Tol}DHP)Co]^+$ (Scheme 2).

We also investigated the regioselectivity of hydrogenation with the substrate trans-2-methyl-1,3-pentene. Here, selectivity for the hydrogenation of the terminal, disubstituted olefin, is observed with ~35% yield, consistent with the reactivity trends from mono-olefinic substrates. Interestingly, the hydrogenated products show cis/trans isomerization as well as migration of the internal double bond to the more thermodynamically favorable tri-substituted position. Given the limited hydrogenation reactivity with internal mono-olefins, we hypothesized that the isomerization of this substrate might be due to a radical pathway for hydrogenation and undertook mechanistic experiments to explore this possibility.

The hydrogenation of α-cyclopropyl styrene as a radical clock test substrate with 10% cat. loading of **2** showed exclusive cyclopropyl ring-opened products, as would be expected for a radical reaction.[26] For this substrate, the major product is doubly hydrogenated *sec*-pentylbenzene in 35(3)% yield. We also observe the tri-substituted olefin product 2-phenylpent-2-ene in 10(2)% yield. This product is the expected intermediate olefin formed after ring-opening. Regardless of the exact product distribution, the absence of any hydrogenated products with an intact cyclopropyl ring strongly suggests a radical mechanism and also suggests related radical reactions to form the observed olefin migration products from trans-2-methyl-1,3-pentene.

Scheme 2. Mechanism for the Synthesis of 3 as well as for the Hydrogenations of Olefins (1-Hexene Used as Model Substrate)

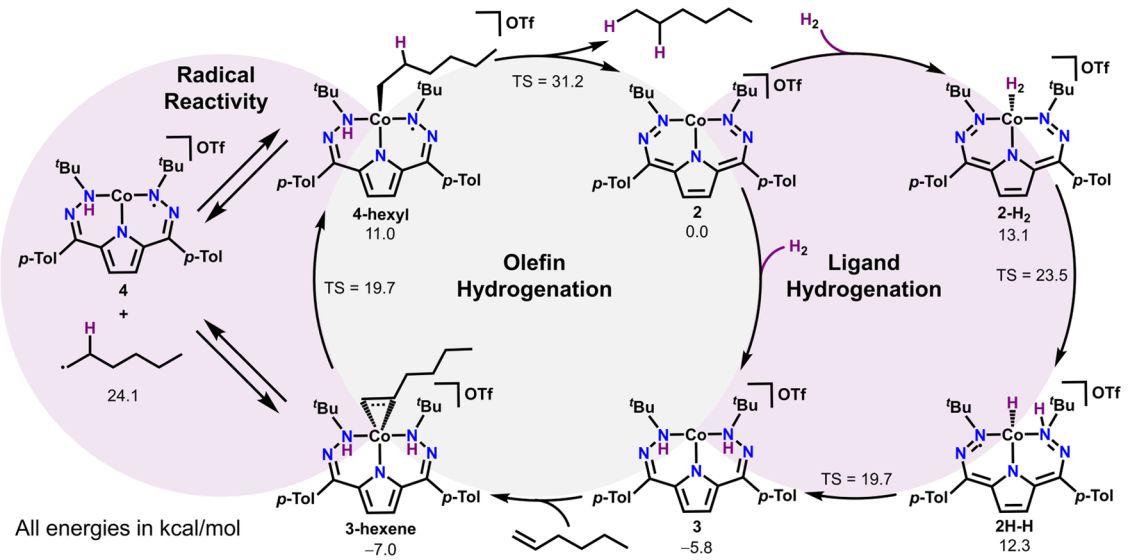

https://doi.org/10.1021/acscatal.2c02467
ACS Catal. 2022, 12, 9933−9943

The agency of radical reactivity in the hydrogenation catalysis of **2** is noteworthy, as Co-based hydrogenation catalysts frequently go through classical organometallic mechanisms featuring Co−H intermediates without radical reactivity.[14g] Indeed, there has been recent interest in discovering Co catalysts with alternative mechanisms, in some cases switched with light.[14g] The absence of any observable Co−H species upon hydrogenation of **2** and the observed radical reactivity in hydrogenation catalysis suggested to us the possibility of an unusual DHP ligand-promoted radical hydrogenation mechanism. While such a mechanism is supported by our experimental data, we also wanted to use DFT calculations to obtain a clearer picture of accessible pathways.

Computational Analysis. All of the experimental data on **3** is consistent with the assignment of a hydrogenated ligand with a Co(II) center generated from the reaction of **2** with H_2. This proposed assignment of **3** and other catalytically relevant intermediates was therefore investigated using DFT calculations (Scheme 2, Figures S56−S57, S64−S65, and S85−S86). Geometry optimizations and frequency calculations for postulated intermediates and transition states along two key cycles, addition of H_2 to the DHP scaffold (Scheme 2 right) as well as 1-hexene hydrogenation (Scheme 2 middle), were calculated using the O3LYP functional and basis sets of def2-SVP on H, def2- TZVPP on Co, and def2-TZVP on N and C atoms (Scheme 2). Both doublet and quartet spin states were considered, and the results suggest that both spin states are relevant for catalysis.

The mechanism to form **3** was investigated both with OTf^- bound to Co and also with an outer sphere (unbound) OTf^-. The transition state energies found for the outer sphere OTf^- pathway are generally lower in energy, sometimes significantly than for reactivity with OTf^- bound to Co. This observation is consistent with the enhanced yields we observe with added $NaBAr_4^F$ as a OTf^- abstractor. The initial hydrogenation of **2** is overall favorable with a free energy of −5.8 kcal/mol. The pathway to form this species goes first 13.1 kcal/mol uphill from **2** through an S = 1/2 Co-H_2 adduct (**2-H_2**). A high-energy transition state between **2-H_2** and an S = 1/2 Co hydride (**2H-H**) with a singly hydrogenated DHP ligand is 23.5 kcal/mol uphill from **2**. Intermediate **2H-H** can then proceed through a low-energy (7.4 kcal/mol versus **2H-H**) transition state to generate **3**.

The DFT-predicted pathway for olefin hydrogenation proceeds through roughly thermoneutral binding of 1-hexene to **3** (−1.2 kcal/mol) to form an S = 3/2 high-spin 1-hexene adduct (**3-hexene**). We then considered two branching pathways from this olefin adduct. Firstly, **3-hexene** could go through an ene-reaction-like transformation to generate a Co-alkyl product, **4-hexyl**. This reaction is unfavorable by 18.0 kcal/mol with a transition state 25.5 kcal/mol uphill in energy from **3-hexene**. We note that the depicted primary product is significantly lower in energy than the formal 2,1 insertion product, likely driven by the sterics of the *t*-Bu groups and thus possibly explaining the preference of the system for terminal olefins. Subsequent loss of alkane and regeneration of **2** proceeds through a high-energy transition state of 31.2 kcal/mol versus **2**. While this pathway is potentially feasible, the facile room-temperature activity of **2** and the observed radical reactivity also prompted us to evaluate separate radical intermediates.

Intermediate **3-hexene** may also transfer an H-atom to the bound 1-hexene to generate a hexyl radical and a singly hydrogenated Co complex **4**. This reaction to generate a terminal hexyl radical is 31.1 kcal/mol uphill in energy from **3-hexene** and is comparable in energy to the highest lying transition state for DHP hydrogenation (30.5 kcal/mol higher than **3-hexene**). The comparatively low energy of these free radical intermediates suggests a very weak Co−C bond in **4-hexyl**, and indeed, the loss of a primary hexyl radical from this intermediate is only 13.1 kcal/mol uphill in energy, and the formation of secondary radicals is even more accessible (Figures S85 and S86). As expected, subsequent H-atom abstraction from **4** by a hexyl radical is extremely favorable.

Without additional experimental details, which are difficult to obtain on this paramagnetic system, it is difficult to determine whether the hexene hydrogenation steps proceed exclusively through Co-bound species, such as **4-hexyl**, or if direct H-atom transfer to generate outer sphere carbon radicals dominates. We suspect that the mechanism features both alkyl radical and metal-alkyl species, which may explain the steric preferences for hydrogenation as well as the radical-derived products observed in mechanistic experiments. Furthermore, we note two additional mechanistic paradigms which deserve discussion. First, while we have limited our discussion to the above cationic pathway with an outer sphere OTf^-, some of the putative intermediates with bound alkyl and OTf^- groups are slightly lower in energy, particularly for the later C−H bond forming steps, suggesting that additional ligation by counterions or solvent may facilitate cycles with bound alkyl substituents (Figures S56 and S57). Second, an additional pathway where intermediate **2H-H** directly binds and inserts olefin may be possible, although we think that the rate of olefin binding to **2H-H**, which would be a bimolecular process, is not likely to be competitive with the low barrier intramolecular reaction to proceed to **3**.

Nevertheless, the computed reaction pathways support the agency of the DHP ligand in hydrogenation and the absence of classic organometallic steps such as insertions from hydride intermediates. The calculations also suggest that improvements on yield or scope might be obtained by reducing the sterics on our catalyst and utilizing a more weakly coordinating anion than OTf^-.

CONCLUSIONS

In this study, we have synthesized a series of Co(II) complexes with the redox-active ^{tBu,Tol}DHP ligand scaffold. The CoOTf complex (**2**) forms a thermally unstable hydrogenated species (**3**) when exposed to dihydrogen, which can be characterized spectroscopically and computationally to confirm its assignment as a Co(II) complex with a hydrogenated DHP ligand. Complex **2** is also a competent catalyst for the hydrogenation of olefins at room temperature with 1 atmosphere of H_2. Catalyst **2** selectively hydrogenates terminal alkenes, and it can also drive rearrangements of olefins into more thermodynamically favored products, likely through radical pathways. The agency of radical intermediates has been confirmed by the ring-opening of the radical clock α-cyclopropyl styrene in hydrogenation reactions. Our results demonstrate that the combination of ligand-based multi-proton and electron storage enables hydrogenation catalysis under mild conditions and, furthermore, that this ligand-centric paradigm enables alternative mechanistic pathways to more classic organometallic catalysts.

https://doi.org/10.1021/acscatal.2c02467
ACS Catal. 2022, 12, 9933−9943

EXPERIMENTAL SECTION

General Methods. All chemicals were purchased from commercial suppliers and used without further purification. All manipulations were carried out under an atmosphere of N_2 using standard Schlenk and glovebox techniques. Glassware was dried at 180 °C for a minimum of 2 h and cooled under vacuum prior to use. Solvents were dried on a solvent purification system from Pure Process Technology and stored over 4 Å molecular sieves under N_2. Tetrahydrofuran (THF) was stirred over NaK alloy and run through an additional alumina column prior to use to ensure dryness. Solvents were tested for H_2O and O_2 using a standard solution of sodium-benzophenone ketyl radical anion. CD_3CN, C_6D_6, and d_8-toluene were dried over 4 Å molecular sieves under N_2. α-cyclopropyl styrene was prepared following a previously reported procedure.[27]

^1H and ^{19}F NMR spectra were recorded on Bruker DRX 400 or 500 spectrometers. Chemical shifts are reported in ppm units referenced to residual solvent resonances for ^1H spectra. UV−visible Spectra were recorded on a Bruker Evolution 300 spectrometer and analyzed using VisionPro software. A standard 1 cm quartz cuvette with an airtight screw cap with a puncturable Teflon seal was used for all measurements. A Unisoku CoolSpek cryostat was used for low-temperature measurements. ^1H and ^{19}F NMR spectra were recorded on either Bruker DRX 400 or AVANCE-500 spectrometers. IR spectra were obtained on a Bruker Tensor II spectrometer with the OPUS software suite. All IR samples were collected between KBr plates. EPR spectra were recorded on an Elexsys E500 Spectrometer with an Oxford ESR 900 X-band cryostat and a Bruker ColdEdge Stinger. EPR data was analyzed using the EasySpin MATLAB suite.[28] Single-crystal X-ray diffraction data was collected in-house using Bruker D8 Venture diffractometer equipped with Mo microfocus X-ray tube (λ = 0.71073 Å).

X-ray near-edge absorption spectra (XANES) were employed to probe the local environment of Co. All sample preparation was performed under an inert atmosphere. Frozen solution samples were prepared by making a concentrated solution of the starting material in toluene (acetonitrile was added for solubility where indicated). This solution was then syringed into a precooled Teflon cuvette lined with Kapton tape in liquid nitrogen and then stored in liquid nitrogen until collection. Data was acquired at the Advanced Photon Source at Argonne National Labs with a bending magnet source with ring energy at 7.00 GeV. Co K-edge data was acquired at the MRCAT 10-BM beamline. The incident, transmitted, and reference X-ray intensities were monitored using gas ionization chambers. A metallic Co foil standard was used as a reference for energy calibration and was measured simultaneously with experimental samples. X-ray absorption spectra were collected at room temperature. Data collected was processed using the Demeter software suite, and Fityk was used for more precise pre-edge fitting.

Co(^{tBu,Tol}DHP)Cl (1). In a 20 mL vial in the glovebox, 1−2 mL of THF was added until the $[^{tBu,Tol}DHP\text{-}H_4][Cl]_2$ ligand sal^{t9c} (0.172 g, 1 equiv 0.333 mmol) dissolved completely as a yellow solution. A concentrated solution of KHMDS (0.186 g, 2.8 equiv, 0.932 mmol) in 1−2 mL THF was added dropwise with stirring. The solution turned from yellow to a bright red color, then darkened to a brownish green upon complete addition. After these color changes and additions were completed, $CoCl_2$ (0.043 g, 1 equiv, 0.331 mmol), suspended in 1−2 mL of THF was added to the reaction mixture, which resulted in a color change to a brown-purple color. 1-hexene (41 μL, 1 equiv, 0.33 mmol) was added, with a resulting color change to a luminous magenta-purple. Shortly after the addition of 1-hexene, the reaction mixture was dried under vacuum to provide a purple solid. This solid was extracted with copious amounts of petroleum ether (50−60 mL). After drying this solution, **1** was obtained as a magenta-purple solid. Yield: 0.134 g, 75%. Single crystals for XRD were grown via cooling a petroleum ether solution at −35 °C. ^1H NMR (400 MHz, C_6D_6, RT): δ = no signals. Magnetic susceptibility: Evans' method (C_6D_6, RT, μ_B): μ_{eff} = 1.74. UV−vis, nm in benzene, (ε, M^{-1} cm^{-1}): 553 (3900). Anal. Calcd C, 62.86; H, 6.41; N, 13.09; found: C, 62.58; H, 5.97; N, 11.46. HRMS (EI) m/z: $[M]^+$ calcd for **1**: $C_{28}H_{34}N_5ClCo$ 534.1835; found, 534.184.

Co(^{tBu,Tol}DHP)OTf (2). In a 20 mL vial in the glovebox, 2 mL of benzene was added to Co(^{Tol,tBu}DHP)Cl (**1**) (0.060 g, 1 equiv, 0.11 mmol). A solution of silver triflate (0.028 g, 1 equiv, 0.11 mmol) in a mixture of 1:1 benzene/acetonitrile (2 mL) was added to the bright purple solution of **1**. The reaction was stirred for 1 h, over which time its color changed from emerald green immediately after addition to an olive color with concomitant formation of gray solids on the sides of the vial. This reaction mixture was dried under vacuum, after which the product was extracted with 10−20 mL of diethyl ether. Yield: 0.065 g, 89%. Single crystals suitable for XRD of **2** were grown out of a concentrated petroleum ether solution at −35 °C. ^1H NMR (400 MHz, C_6D_6, RT): δ = 24.20 (bs), 10.17 (s), 9.07 (bs), 7.36 (s), 6.96(s), 6.87(bs), 4.06 (s). Magnetic susceptibility: Evans' method for **2** (C_6D_6, RT, μ_B): μ_{eff} = 1.71, UV−vis, nm in toluene, (ε, $M^{-1}cm^{-1}$): 516 (3700). Anal. Calcd C, 53.70; H, 5.28; N, 10.80; found, 54.32, 5.55, 10.31. HRMS (EI) m/z: $[M]^+$ cald for **2**: $C_{29}H_{34}N_5O_3F_3S$ Co 648.1666; found, 648.1665.

Reactivity with H_2. A 100 mL Schlenk flask with 8 mg of **2** with 50−100 μL of toluene was prepared in the glovebox. This solution was frozen in liquid nitrogen, and the headspace was evacuated under vacuum. The flask was then backfilled with 1 atm of H_2, which is equivalent to ∼3.8 atm of H_2 at room temperature. The flask was then relocated into a freezer at −25 °C, where it was allowed to react for 30−36 h without stirring. Upon completion of the reaction with H_2, the reddish-purple color of **2** converts to a pinker purple, indicating the formation of **3**. Complex **3** is stable to vacuum and is relatively stable as a solid to air but decomposes rapidly if exposed to air in the solution state. This complex is relatively stable below 0 °C, but slow decomposition occurs at this temperature and above. To characterize this product, the reaction vessel was pumped back into the nitrogen-filled glovebox and placed into a −35 °C freezer. The cold solution was then dried rapidly under vacuum and then analyzed by various techniques, as described below. IR (Nujol mull between KBr plates, cm^{-1}): 3180 (N−H, w), 3170 (N−H, w), 1641 (s).

Preparation of IR samples of 3. *Nujol Mull.* Complex **3** (8 mg), prepared in the method described above, was mixed in a cold mortar and pestle with minimal nujol to form a mustard-like suspension. This mixture was dolloped on a cooled KBr plate, and a second plate was placed on top. The sample was then transferred in an air-free temporary container to the spectrometer, and a spectrum was collected.

Thin Film on KBr Plate. Complex **3** (8 mg), prepared in the method described above, was dissolved in cold, dry diethyl

https://doi.org/10.1021/acscatal.2c02467
ACS Catal. 2022, 12, 9933−9943

ether to form a concentrated solution. This was dropped on a cooled KBr plate, and a second plate was placed on top. The sample was then transferred in an air-free temporary container to the spectrometer, and a spectrum was collected.

General Catalytic Hydrogenation Procedures and Products. *Procedure for 1% Loading.* In a nitrogen-filled glovebox, a 250 mL Schlenk flask with a magnetic stir bar was charged with unsaturated substrate (0.077 mmol, 100 equiv), **2** (0.0005 g, 0.0008 mmol), mesitylene (0.002 mL, 0.014 mmol) (internal standard), and benzene-d_6 (0.1 mL). On a Schlenk line, the solution was freeze−pump−thaw-degassed and warmed to room temperature with the contents under static vacuum. At room temperature, this vessel was backfilled with 1 atm H_2 gas. The vessel was then sealed and left to stir for 18 h. The dark red-purple **1** could be observed to pinken within the hour, turn greenish-red, and then begin to turn orange/yellow after 6 h. After 18 h, the vessel was shipped back into the nitrogen-filled glovebox and diluted to 0.7 mL total volume. This was then analyzed via ^{1}H and ^{19}F NMR, and checked by GC-MS as needed.

Procedure for 2.5% Loading. The general method described above was implemented with 0.031 mmol, 40 equiv of unsaturated solvent used.

Procedure for 2.5% Loading with $NaBAr_4^F$. The general method described above was implemented with 0.031 mmol, 40 equiv of unsaturated solvent used and with the addition of 0.0008 mmol, 1 equiv of $NaBAr_4^F$ pre-added to the reaction vessel with 0.07 mL of THF.

Procedure for 10% Loading. In a nitrogen-filled glovebox, a 250 mL Schlenk flask with a magnetic stir bar was charged with unsaturated substrate (0.0077 mmol, 10 equiv), **2** (0.0005 g, 0.0008 mmol), mesitylene (0.002 mL, 0.014 mmol) (internal standard), and benzene-d_6 (0.1 mL). On a Schlenk line, the solution was freeze−pump−thaw-degassed and backfilled at 77 K with 3.8 atm H_2 gas. The vessel was then sealed and left to stir for 18 h. After 18 h, the vessel was shipped back into the nitrogen-filled glovebox and diluted to 0.7 mL total volume. This was then analyzed via ^{1}H and ^{19}F NMR and checked by GC-MS as needed.

■ ASSOCIATED CONTENT

Supporting Information

The Supporting Information is available free of charge at https://pubs.acs.org/doi/10.1021/acscatal.2c02467.

Experimental procedures, NMR, IR, GC-MS UV−vis, EPR, XAS, SXRD data, and DFT (PDF)

Crystallographic Data 1 (CIF)

Crystallographic Data 2 (CIF)

(PDF)

(CIF)

(CIF)

Accession Codes

CCDC 2173743 and 2173744 contain the supplementary crystallographic data for this paper. This data can be obtained free of charge via www.ccdc.cam.ac.uk/data_request/cif, or by emailing to data_request@ccdc.cam.ac.uk, or by contacting The Cambridge Crystallographic Data Centre, 12 Union Road, Cambridge CB2 1EZ, UK; fax: +44 1223 336033

■ AUTHOR INFORMATION

Corresponding Author

John S. Anderson − *Department of Chemistry, The University of Chicago, Chicago, Illinois 60627, United States;* orcid.org/0000-0002-0730-3018; Email: jsanderson@uchicago.edu

Authors

Sophie W. Anferov − *Department of Chemistry, The University of Chicago, Chicago, Illinois 60627, United States*

Alexander S. Filatov − *Department of Chemistry, The University of Chicago, Chicago, Illinois 60627, United States;* orcid.org/0000-0002-8378-1994

Complete contact information is available at: https://pubs.acs.org/10.1021/acscatal.2c02467

Author Contributions

All authors have given approval to the final version of the manuscript.

Notes

The authors declare no competing financial interest.

■ ACKNOWLEDGMENTS

This work was supported by the National Institutes of Health (R35 GM133470). The authors thank the University of Chicago for funding, the 3M Corporation for a NTFA to J.S.A., and the Sloan Foundation for a Research Fellowship to J.S.A. (FG-2019-11497). The authors also thank the Research Computing Center at the University of Chicago for providing computing resources. Some data reported here was collected at MRCAT. MRCAT operations are supported by the Department of Energy and the MRCAT member institutions. This research used resources of the Advanced Photon Source, a U.S. Department of Energy (DOE) Office of Science User Facility operated for the DOE Office of Science by Argonne National Laboratory under Contract No. DE-AC02-06CH11357. The authors thank Dr. John Katsoudas and Dr. Joshua Wright for assistance with XAS collection at beamline 10-BM. The authors would like to thank A. Anferov for assistance building their XAS set-up, and Dr. K. Jesse for valuable input. The authors would like to thank S.J. and M.W. for helpful discussions.

■ REFERENCES

(1) (a) Crabtree, R. H. *Organometallic Chemistry of the Transition Metals*, 6th ed.; 2014; pp 55−56. (b) Wen, J.; Wang, F.; Zhang, X. Asymmetric hydrogenation catalyzed by first-row transition metal complexes. *Chem. Soc. Rev.* **2021**, *50*, 3211−3237.

(2) (a) Ito, N.; Phillips, S. E. V.; Stevens, C.; Ogel, Z. B.; McPherson, M. J.; Keen, J. N.; Yadav, K. D. S.; Knowles, P. F. Novel thioether bond revealed by a 1.7 Å crystal structure of galactose oxidase. *Nature* **1991**, *350*, 87−90. (b) Ito, N.; Phillips, S. E. V.; Stevens, C.; Ogel, Z. B.; McPherson, M. J.; Keen, J. N.; Yadav, K. D. S.; Knowles, P. F. Three-dimensional structure of galactose oxidase: an enzyme with a built-in secondary cofactor. *Faraday Discuss.* **1992**, *93*, 75. (c) Branchaud, B. P.; Montagne-Smith, M. P.; Kosman, D. J.; McLaren, F. R. Mechanism-based inactivation of galactose oxidase: evidence for a radical mechanism. *J. Am. Chem. Soc.* **1993**, *115*, 798. (d) Whittaker, M. M.; Whittaker, J. M. Ligand interactions with galactose oxidase: mechanistic insights. *Biophys. J.* **1993**, *64*, 762. (e) Ito, N.; Phillips, S. E. V.; Yadav, K. D. S.; Knowles, P. F. Crystal structure of a free radical enzyme, galactose oxidase. *J. Mol. Biol.* **1994**, *238*, 794. (f) Knowles, P. F.; Ito, N.*Perspectives in Bio-inorganic Chemistry*, Jai Press Ltd., 1994; Vol. 2, pp 207−244. (g) Wachter, R.

M.; Branchaud, B. P. Molecular modeling studies on oxidation of hexopyranoses by galactose oxidase. An active site topology apparently designed to catalyze radical reactions, either concerted or stepwise. *J. Am. Chem. Soc.* **1996**, *118*, 2782. (h) Wachter, R. M.; Montagne-Smith, M. P.; Branchaud, B. P. β-Haloethanol substrates as probes for radical mechanisms for galactose oxidase. *J.Am. Chem. Soc.* **1997**, *119*, 7743. (i) Whittaker, M. M.; Ballou, D. P.; Whittaker, J. W. Kinetic isotope effects as probes of the mechanism of galactose oxidase. *Biochemistry* **1998**, *37*, 8426. (j) Whittaker, J. W.; Whittaker, M. M. Radical copper oxidases, one electron at a time. *Pure Appl. Chem.* **1998**, *70*, 903. (k) Chaudhuri, P.; Hess, M.; Müller, J.; Hildenbrand, K.; Bill, E.; Weyhermüller, T.; Wieghardt, K. Aerobic oxidation of primary alcohols (including methanol) by Copper (II)− and Zinc (II)− phenoxyl radical catalysts. *J. Am. Chem. Soc.* **1999**, *121*, 9599−9610. (l) Cook, S. A.; Hill, E. A.; Borovik, A. S. Lessons from nature: a bio-inspired approach to molecular design. *Biochemistry* **2015**, *54*, 4167−4180. (m) Baumgardner, D. F.; Parks, W. E.; Gilbertson, J. D. Harnessing the active site triad: merging hemilability, proton responsivity, and ligand-based redox-activity. *Dalton Trans.* **2020**, *49*, 960−965.

(3) Cook, S. A.; Borovik, A. S. Molecular designs for controlling the local environments around metal ions. *Acc. Chem. Res.* **2015**, *48*, 2407−2414.

(4) (a) Rakowski Dubois, M.; Dubois, D. L. Development of Molecular Electrocatalysts for CO2 Reduction and H2 Production/Oxidation. *Acc. Chem. Res.* **2009**, *42*, 1974−1982. (b) Zell, T.; Milstein, D. Hydrogenation and dehydrogenation iron pincer catalysts capable of metal−ligand cooperation by aromatization/dearomatization. *Acc. Chem. Res.* **2015**, *48*, 1979−1994. (c) Pegis, M. L.; Wise, C. F.; Martin, D. J.; Mayer, J. M. Oxygen reduction by homogeneous molecular catalysts and electrocatalysts. *Chem. Rev.* **2018**, *118*, 2340−2391.

(5) (a) Luca, O. R.; Crabtree, R. H. Redox-active ligands in catalysis. *Chem. Soc. Rev.* **2013**, *42*, 1440−1459. (b) Arevalo, R.; Chirik, P. J. Enabling two-electron pathways with iron and cobalt: from ligand design to catalytic applications. *J. Am. Chem. Soc.* **2019**, *141*, 9106−9123. (c) Ott, J. C.; Bürgy, D.; Guan, H.; Gade, L. H. 3d Metal Complexes in T-shaped Geometry as a Gateway to Metalloradical Reactivity. *Acc. Chem. Res.* **2022**, *55*, 857−868.

(6) (a) Käß, M.; Friedrich, A.; Drees, M.; Schneider, S. Ruthenium Complexes with Cooperative PNP Ligands: Bifunctional Catalysts for the Dehydrogenation of Ammonia−Borane. *Angew. Chem., Int. Ed.* **2009**, *48*, 905−907. (b) Khaskin, E.; Iron, M. A.; Shimon, L. J. W.; Zhang, J.; Milstein, D. N− H activation of amines and ammonia by Ru via metal− ligand cooperation. *J. Am. Chem. Soc.* **2010**, *132*, 8542. (c) Feller, M.; Diskin-Posner, Y.; Shimon, L. J. W.; Ben-Ari, E.; Milstein, D. N−H Activation by Rh (I) via Metal−Ligand Cooperation. *Organometallics* **2012**, *31*, 4083. (d) He, L. P.; Chen, T.; Gong, D.; Lai, Z.; Huang, K. W. Enhanced reactivities toward amines by introducing an imine arm to the pincer ligand: direct coupling of two amines to form an imine without oxidant. *Organometallics* **2012**, *31*, 5208. (e) Rodríguez-Lugo, R. E.; Trincado, M.; Vogt, M.; Tewes, F.; Santiso-Quinones, G.; Grützmacher, H. A homogeneous transition metal complex for clean hydrogen production from methanol−water mixtures. *Nat. Chem.* **2013**, *5*, 342−347. (f) Myers, T. W.; Berben, L. A. Aluminum−ligand cooperative N−H bond activation and an example of dehydrogenative coupling. *J. Am. Chem. Soc.* **2013**, *135*, 9988−9990. (g) Xu, R.; Chakraborty, S.; Bellows, S. M.; Yuan, H.; Cundari, T. R.; Jones, W. D. Iron-Catalyzed Homogeneous Hydrogenation of Alkenes under Mild Conditions by a Stepwise, Bifunctional Mechanism. *ACS Catal.* **2016**, *6*, 2127−2135. (h) Sherbow, T. J.; Fettinger, J. C.; Berben, L. A. Control of Ligand pKa Values Tunes the Electrocatalytic Dihydrogen Evolution Mechanism in a Redox-Active Aluminum(III) Complex. *Inorg. Chem.* **2017**, *56*, 8651−8660. (i) Rajabimoghadam, K.; Darwish, Y.; Bashir, Y.; Pirman, D.; Eichelberger, S.; Sieler, M. A.; Swart, M.; Garcia-Bosch, I. Catalytic aerobic oxidation of alcohols by copper complexes bearing redox-active ligands with tunable H-bonding groups. *J. Am. Chem. Soc.* **2018**, *140*, 16625−16634. (j) Sinha, S.; Das, S.; Mondal, R.; Mandal, S.; Paul, N. D. Cobalt complexes of redox noninnocent azo-aromatic pincers. Isolation, characterization, and application as catalysts for the synthesis of quinazolin-4 (3 H)-ones. *Dalton Trans.* **2020**, *49*, 8448−8459.

(7) (a) Thompson, E. J.; Berben, L. A. Electrocatalytic Hydrogen Production by an Aluminum (III) Complex: Ligand-Based Proton and Electron Transfer. *Angew. Chem., Int. Ed.* **2015**, *54*, 11642−11646. (b) Margulieux, G. W.; Bezdek, M. J.; Turner, Z. R.; Chirik, P. J. Ammonia Activation, H2 Evolution and Nitride Formation from a Molybdenum Complex with a Chemically and Redox Noninnocent Ligand. *J. Am. Chem. Soc.* **2017**, *139*, 6110−6113. (c) Dauth, A.; Gellrich, U.; Diskin-Posner, Y.; Ben-David, Y.; Milstein, D. The ferraquinone−ferrahydroquinone couple: combining quinonic and metal-based reactivity. *J. Am. Chem. Soc.* **2017**, *139*, 2799−2807. (d) Rosenkoetter, K. E.; Wojnar, M. K.; Charette, B. J.; Ziller, J. W.; Heyduk, A. F. Hydrogen-atom noninnocence of a tridentate [SNS] pincer ligand. *Inorg. Chem.* **2018**, *57*, 9728−9737. (e) Ward, M. B.; Scheitler, A.; Yu, M.; Senft, L.; Zillmann, A. S.; Gorden, J. D.; Schwartz, D. D.; Ivanović-Burmazović, D. D.; Goldsmith, C. R. Superoxide dismutase activity enabled by a redox-active ligand rather than metal. *Nat. Chem.* **2018**, *10*, 1207−1212. (f) Alig, L.; Fritz, M.; Schneider, S. First-Row Transition Metal (De)Hydrogenation Catalysis Based On Functional Pincer Ligands. *Chem. Rev.* **2019**, *119*, 2681−275. (g) Drummond, M. J.; Ford, C. L.; Gray, D. L.; Popescu, C. V.; Fout, A. R. Radical Rebound Hydroxylation Versus H-Atom Transfer in Non-Heme Iron(III)-Hydroxo Complexes: Reactivity and Structural Differentiation. *J. Am. Chem. Soc.* **2019**, *141*, 6639−6650.

(8) (a) Purse, B. W.; Tran, L.-H.; Piera, J.; Åkermark, B.; Bäckvall, J.-E. Bäckvall, Synthesis of New Hybrid Hydroquinone/Cobalt Schiff Base Catalysts: Efficient Electron-Transfer Mediators in Aerobic Oxidation. *Chem. − Eur. J.* **2008**, *14*, 7500−7503. (b) Myers, T. W.; Berben, L. A. Aluminium−ligand cooperation promotes selective dehydrogenation of formic acid to H2 and CO2. *Chem. Sci.* **2014**, *5*, 2771−2777. (c) Henthorn, J. T.; Lin, S.; Agapie, T. Combination of Redox-Active Ligand and Lewis Acid for Dioxygen Reduction with π-Bound Molybdenum− Quinonoid Complexes. *J. Am. Chem. Soc.* **2015**, *137*, 1458−1464. (d) Lagaditis, P. O.; Schluschaß, B.; Demeshko, S.; Würtele, C.; Schneider, S. Square-Planar Cobalt (III) Pincer Complex. *Inorg. Chem.* **2016**, *55*, 4529−4536. (e) Schneck, F.; Finger, M.; Tromp, M.; Schneider, S. Chemical Non-Innocence of an Aliphatic PNP Pincer Ligand. *Chem. − Eur. J.* **2017**, *23*, 33−37. (f) Lindley, B. M.; Bruch, Q. J.; White, P. S.; Hasanayn, F.; Miller, A. J. M. Ammonia Synthesis from a Pincer Ruthenium Nitride via Metal−Ligand Cooperative Proton-Coupled Electron Transfer. *J. Am. Chem. Soc.* **2017**, *139*, 5305−5308. (g) Pramanick, R.; Bhattacharjee, R.; Sengupta, D.; Datta, A.; Goswami, S. An azoaromatic ligand as four electron four proton reservoir: catalytic dehydrogenation of alcohols by its zinc (II) complex. *Inorg. Chem.* **2018**, *57*, 6816−6824. (h) Jain, R.; Mamun, A. A.; Buchanan, R. M.; Kozlowski, P. M.; Grapperhaus, C. A. Ligand-assisted metal-centered electrocatalytic hydrogen evolution upon reduction of a bis (thiosemicarbazonato) Ni (II) complex. *Inorg. Chem.* **2018**, *57*, 13486−13493. (i) Sherbow, T. J.; Thompson, E. J.; Arnold, A.; Sayler, R. I.; Britt, R. D.; Berben, L. A. Electrochemical Reduction of N2 to NH3 at Low Potential by a Molecular Aluminum Complex. *Chem. − Eur. J* **2019**, *25*, 454−458.

(9) (a) Chang, M.-C.; McNeece, A. J.; Hill, E. A.; Filatov, A. S.; Anderson, J. S. Ligand-Based Storage of Protons and Electrons in Dihydrazonopyrrole Complexes of Nickel. *Chem. − Eur. J.* **2018**, *24*, 8001−8008. (b) Chang, M.-C.; Jesse, K. A.; Filatov, A. S.; Anderson, J. S. Reversible homolytic activation of water via metal−ligand cooperativity in a T-shaped Ni (ii) complex. *Chem. Sci.* **2019**, *10*, 1360−1367. (c) McNeece, A. J.; Jesse, K. A.; Xie, J.; Filatov, A. S.; Anderson, J. S. Generation and Oxidative Reactivity of a Ni (II) Superoxo Complex via Ligand-Based Redox Non-Innocence. *J. Am. Chem. Soc.* **2020**, *142*, 10824−10832.

https://doi.org/10.1021/acscatal.2c02467
ACS Catal. 2022, 12, 9933−9943

(10) McNeece, A. J.; Jesse, K. A.; Filatov, A. S.; Schneider, J. E.; Anderson, J. S. Catalytic hydrogenation enabled by ligand-based storage of hydrogen. *Chem. Commun.* **2021**, *57*, 3869−3872.
(11) Jesse, K. A.; Anferov, S. W.; Collins, K. A.; Valdez-Moriera, J. A.; Czaikowski, M. E.; Filatov, A. S.; Anderson, J. S. Direct Aerobic Generation of a Ferric Hydroperoxo Intermediate Via a Preorganized Secondary Coordination Sphere. *J. Am. Chem. Soc.* **2021**, *143*, 18121−18130.
(12) (a) Fryzuk, M. D.; Leznoff, D. B.; Thompson, R. C.; Rettig, S. J. One-electron transformations of paramagnetic cobalt complexes. Synthesis and structure of cobalt (II) amidodiphosphine halide and alkyl complexes and their reaction with alkyl halides. *J. Am. Chem. Soc.* **1998**, *120*, 10126−10135. (b) Lyaskovskyy, V.; de Bruin, B. Redox non-innocent ligands: versatile new tools to control catalytic reactions. *ACS Catal.* **2012**, *2*, 270−279. (c) Zhang, G.; Hanson, S. K. Cobalt-catalyzed transfer hydrogenation of C=O and C=N bonds. *Chem. Commun.* **2013**, *49*, 10151−10153. (d) Zhang, G.; Vasudevan, K. V.; Scott, B. L.; Hanson, S. K. Understanding the mechanisms of cobalt-catalyzed hydrogenation and dehydrogenation reactions. *J. Am. Chem. Soc.* **2013**, *135*, 8668−8681. (e) Jing, Y.; Chen, X.; Yang, X. Computational mechanistic study of the hydrogenation and dehydrogenation reactions catalyzed by cobalt pincer complexes. *Organometallics* **2015**, *34*, 5716−5722. (f) Fu, S.; Chen, N.-Y.; Liu, X.; Shao, Z.; Luo, S.-P.; Liu, Q. Ligand-Controlled Cobalt-Catalyzed Transfer Hydrogenation of Alkynes: Stereodivergent Synthesis of Z- and E-Alkenes. *J. Am. Chem. Soc.* **2016**, *138*, 8588−8594. (g) Qi, X.; Liu, X.; Qu, L.-B.; Liu, Q.; Lan, Y. Mechanistic insight into cobalt-catalyzed stereodivergent semihydrogenation of alkynes: The story of selectivity control. *J. Catal.* **2018**, *362*, 25−34. (h) Liu, X.; Zhang, W.; Wang, Y.; Zhang, Z.-X.; Jiao, L.; Liu, Q. Cobalt-catalyzed regioselective olefin isomerization under kinetic control. *J. Am. Chem. Soc.* **2018**, *140*, 6873−6882. (i) Merz, L. S.; Blasius, C. K.; Wadepohl, H.; Gade, L. H. Square planar cobalt (II) hydride versus T-shaped cobalt (I): structural characterization and dihydrogen activation with PNP−cobalt pincer complexes. *Inorg. Chem.* **2019**, *58*, 6102−6113. (j) Ai, W.; Zhong, R.; Liu, X.; Liu, Q. Hydride transfer reactions catalyzed by cobalt complexes. *Chem. Rev.* **2019**, *119*, 2876−2953. (k) Sang, S.; Unruh, T.; Demeshko, S.; Domenianni, L. I.; van Leest, N. P.; Marquetand, P.; Schneck, F.; Würtele, C.; de Zwart, F. J.; de Bruin, B.; González, L.; Vöhringer, P.; Schneider, S. Photo-Initiated Cobalt-Catalyzed Radical Olefin Hydrogenation. *Chem. − Eur. J.* **2021**, *27*, 16978−16989.
(13) (a) Kooistra, T. M.; Knijnenburg, Q.; Smits, J. M. M.; Horton, A. D.; Budzelaar, P. H. M.; Gal, A. W. Olefin Polymerization with [{bis(imino)pyridyl}$Co^{II}Cl_2$]: Generation of the Active Species Involves Co^{I}. *Angew. Chem., Int. Ed.* **2001**, *40*, 4719−4722. (b) Knijnenburg, Q.; Hetterscheid, D.; Kooistra, T. M.; Budzelaar, P. H. M. The Electronic Structure of (Diiminopyridine)cobalt(I) Complexes. *Eur. J. Inorg. Chem.* **2004**, *2004*, 1204−1211. (c) Knijnenburg, Q.; Horton, A. D.; Heijden, H. V. d.; Kooistra, T. M.; Hetterscheid, D. G. H.; Smits, J. M. M.; Bruien, B. D.; Budzelaar, P. H. M.; Gal, A. W. Olefin hydrogenation using diimine pyridine complexes of Co and Rh. *J. Mol. Catal. A: Chem.* **2005**, *232*, 151−159. (d) Hopmann, K. H. Cobalt−bis (imino) pyridine-catalyzed asymmetric hydrogenation: electronic structure, mechanism, and stereoselectivity. *Organometallics* **2013**, *32*, 6388−6399. (e) Guo, J.; Cheng, B.; Shen, X.; Lu, Z. Cobalt-catalyzed asymmetric sequential hydroboration/hydrogenation of internal alkynes. *J. Am. Chem. Soc.* **2017**, *139*, 15316−15319.
(14) (a) Monfette, S.; Turner, Z. R.; Semproni, S. P.; Chirik, P. J. Enantiopure C1-Symmetric Bis(imino)pyridine Cobalt Complexes for Asymmetric Alkene Hydrogenation. *J. Am. Chem. Soc.* **2012**, *134*, 4561−4564. (b) Yu, R. P.; Darmon, J. M.; Milsmann, C.; Daut, G. W.; Stieber, S. C. E.; DeBeer, S.; Chirik, P. J. Catalytic hydrogenation activity and electronic structure determination of bis (arylimidazol-2-ylidene) pyridine cobalt alkyl and hydride complexes. *J. Am. Chem. Soc.* **2013**, *135*, 13168. (c) Semproni, S. P.; Milsmann, C.; Chirik, P. J. *J. Am. Chem. Soc.* **2014**, *136*, 9211−9224. (d) Chirik, P. J. Iron-and cobalt-catalyzed alkene hydrogenation: catalysis with both redox-active and strong field ligands. *Acc. Chem. Res.* **2015**, *48*, 1687−1695. (e) Friedfeld, M. R.; Shevlin, M.; Margulieux, G. W.; Campeau, L.-C.; Chirik, P. J. Cobalt-catalyzed enantioselective hydrogenation of minimally functionalized alkenes: isotopic labeling provides insight into the origin of stereoselectivity and alkene insertion preferences. *J. Am. Chem. Soc.* **2016**, *138*, 3314−3324. (f) Viereck, P.; Krautwald, S.; Pabst, T. P.; Chirik, P. J. A boron activating effect enables cobalt-catalyzed asymmetric hydrogenation of sterically hindered alkenes. *J. Am. Chem. Soc.* **2020**, *142*, 3923−3930. (g) Mendelsohn, L. N.; MacNeil, C. S.; Tian, L.; Park, Y.; Scholes, G. D.; Chirik, P. J. Visible-Light-Enhanced Cobalt-Catalyzed Hydrogenation: Switchable Catalysis Enabled by Divergence between Thermal and Photochemical Pathways. *ACS Catal.* **2021**, *11*, 1351−1360.
(15) (a) Zhang, G.; Scott, B. L.; Hanson, S. K. Mild and Homogeneous Cobalt-Catalyzed Hydrogenation of C=C, C=O, and C=N Bonds. *Angew. Chem., Int. Ed.* **2012**, *51*, 12102−12106. (b) Lin, T. P.; Peters, J. C. Boryl−metal bonds facilitate cobalt/nickel-catalyzed olefin hydrogenation. *J. Am. Chem. Soc.* **2014**, *136*, 13672−13683.
(16) (a) Yang, L.; Powell, D. R.; Houser, R. P. Structural variation in copper(i) complexes with pyridylmethylamide ligands: structural analysis with a new four-coordinate geometry index, $\tau 4$. *Dalton Trans.* **2007**, 955. (b) Okuniewski, A.; Rosiak, D.; Chojnacki, J.; Becker, B. Coordination polymers and molecular structures among complexes of mercury (II) halides with selected 1-benzoylthioureas. *Polyhedron.* **2015**, *90*, 47−57.
(17) Bowman, A. C.; Milsmann, C.; Bill, E.; Lobkovsky, E.; Weyhermüller, T.; Wieghardt, K.; Chirik, P. J. Reduced N-Alkyl Substituted Bis(imino)pyridine Cobalt Complexes: Molecular and Electronic Structures for Compounds Varying by Three Oxidation States. *Inorg. Chem.* **2010**, *49*, 6110−6123.
(18) Jensen, K. P.; Ryde, U. Comparison of the chemical properties of iron and cobalt porphyrins and corrins. *ChemBioChem* **2003**, *4*, 413−424.
(19) Addison, A. W.; Rao, N. T.; Reedijk, J.; van Rijn, J.; Verschoor, G. C. Synthesis, structure, and spectroscopic properties of copper(II) compounds containing nitrogen−sulphur donor ligands; the crystal and molecular structure of aqua[1,7-bis(N-methylbenzimidazol-2′-yl)-2,6-dithiaheptane]copper(II) perchlorate. *J. Chem. Soc., Dalton Trans.* **1984**, *7*, 1349−1356.
(20) (a) Scott, J.; Gambarotta, S.; Korobkov, I.; Knijnenburg, Q.; de Bruin, B.; Budzelaar, P. H. M. Formation of a Paramagnetic Al Complex and Extrusion of Fe during the Reaction of (Diiminepyridine)Fe with AlR3 (R = Me, Et). *J. Am. Chem. Soc.* **2005**, *127*, 17204. (b) Bowman, A. C.; Milsmann, C.; Atienza, C. C. H.; Lobkovsky, E.; Wieghardt, K.; Chirik, P. J. Synthesis and molecular and electronic structures of reduced bis (imino) pyridine cobalt dinitrogen complexes: ligand versus metal reduction. *J. Am. Chem. Soc.* **2010**, *132*, 1676. (c) Milsmann, C.; Turner, Z. R.; Semproni, S. P.; Chirik, P. J. Azo N= N Bond Cleavage with a Redox-Active Vanadium Compound Involving Metal−Ligand Cooperativity. *Angew. Chem., Int. Ed.* **2012**, *51*, 5386. (d) Yu, R. P.; Darmon, J. M.; Milsmann, C.; Margulieux, G. W.; Stieber, S. C. E.; DeBeer, S.; Chirik, P. J. Catalytic hydrogenation activity and electronic structure determination of bis (arylimidazol-2-ylidene) pyridine cobalt alkyl and hydride complexes. *J. Am. Chem. Soc.* **2013**, *135*, 13168−13184.
(21) (a) Poddel'sky, A. I.; Cherkasov, V. K.; Abakumov, G. A. Transition metal complexes with bulky 4, 6-di-tert-butyl-N-aryl (alkyl)-o-iminobenzoquinonato ligands: Structure, EPR and magnetism. *Coord. Chem. Rev.* **2009**, *253*, 291−324. (b) Goswami, M.; Lyaskovskyy, V.; Domingos, S. R.; Buma, W. J.; Woutersen, S.; Troeppner, O.; Ivanović-Burmazović, I.; Lu, H.; Cui, S.; Zhang, X. P.; Reijerse, E. J.; DeBeer, S.; van Schooneveld, M. M.; Pfaff, F. F.; Ray, K.; de Bruin, Bas. Characterization of porphyrin-Co (III)-'nitrene radical'species relevant in catalytic nitrene transfer reactions. *J. Am. Chem. Soc.* **2015**, *137*, 5468−5479. (c) Kuijpers, P. F.; van der Vlugt, J. I.; Schneider, S.; de Bruin, B. Nitrene radical intermediates in catalytic synthesis. *Chem. — Eur. J.* **2017**, *23*, 13819−13829. (d) Jiang, H.; Lang, K.; Lu, H.; Wojtas, L.; Zhang, X. P. Asymmetric

https://doi.org/10.1021/acscatal.2c02467
ACS Catal. 2022, 12, 9933−9943

radical bicyclization of allyl azidoformates via cobalt (II)-based metalloradical catalysis. *J. Am. Chem. Soc.* **2017**, *139*, 9164−9167. (e) Reckziegel, A.; Kour, M.; Battistella, B.; Mebs, S.; Beuthert, K.; Berger, R.; Werncke, C. G. High-Spin Imido Cobalt Complexes with Imidyl Radical Character. *Angew. Chem., Int. Ed.* **2021**, *60*, 15376.

(22) (a) Hay-Motherwell, R. S.; Wilkinson, G.; Hussain, B.; Hursthouse, M. B. Alkyl complexes of cobalt (II). X-ray crystal structures of (Me2NCH2CH2NMe2) CoR2, R= CH2SiMe3, CH2CMe3,[(Me2NCH2CH2NMe2) Li] 2 [Co (CH2SiMe3) 4] and [(Me2NCH2CH2NMe2) 2Li][CoCl {CH (SiMe3) 2} 2]. *Polyhedron* **1990**, *9*, 931. (b) Scott, J.; Gambarotta, S.; Korobkov, I.; Knijnenburg, Q.; de Bruin, B.; Budzelaar, P. H. M. Formation of a Paramagnetic Al Complex and Extrusion of Fe during the Reaction of (Diiminepyridine)Fe with AlR3 (R = Me, Et). *J. Am. Chem. Soc.* **2005**, *127*, 17204. (c) Bowman, A. C.; Milsmann, C.; Atienza, C. C. H.; Lobkovsky, E.; Wieghardt, K.; Chirik, P. J. Synthesis and molecular and electronic structures of reduced bis (imino) pyridine cobalt dinitrogen complexes: ligand versus metal reduction. *J. Am. Chem. Soc.* **2010**, *132*, 1676. (d) Mo, Z.; Li, Y.; Lee, H. K.; Deng, L. Square-Planar Cobalt Complexes with Monodentate N-Heterocyclic Carbene Ligation: Synthesis, Structure, and Catalytic Application. *Organometallics* **2011**, *30*, 4687. (e) Bowman, A. C.; Milsmann, C.; Bill, E.; Turner, Z. R.; Lobkovsky, E.; DeBeer, S.; Wieghardt, K.; Chirik, P. J. Synthesis and Electronic Structure Determination of N-Alkyl-Substituted Bis(imino)pyridine Iron Imides Exhibiting Spin Crossover Behavior. *J. Am. Chem. Soc.* **2011**, *133*, 17353.

(23) (a) Jenkins, D. M.; Di Bilio, A. J.; Allen, M. J.; Betley, T. A.; Peters, J. C. Elucidation of a low spin cobalt (II) system in a distorted tetrahedral geometry. *J. Am. Chem. Soc.* **2002**, *124*, 15336−15350. (b) Harris, C. F.; Bayless, M. B.; van Leest, N. P.; Bruch, Q. J.; Livesay, B. N.; Bacsa, J.; Hardcastle, K. I.; Shores, M. P.; de Bruin, B.; Soper, J. D. Redox-Active Bis (phenolate) N-Heterocyclic Carbene [OCO] Pincer Ligands Support Cobalt Electron Transfer Series Spanning Four Oxidation States. *Inorg. Chem.* **2017**, *56*, 12421−12435. (c) Liu, Y.; Du, J.; Deng, L. Synthesis, Structure, and Reactivity of Low-Spin Cobalt(II) Imido Complexes [(Me3P)3Co-(NAr)]. *Inorg. Chem.* **2017**, *56*, 8278−8286. (d) Spillecke, L.; Tripathi, S.; Koo, C.; Bahr, A.; Swain, A.; Haldar, R.; Ansari, M.; Jasinski, J.; Rajaraman, G.; Shanmugam, M.; Klingeler, R. Role of Coordination Geometry on the Magnetic Relaxation Dynamics of Isomeric Five-Coordinate Low-Spin Co (II) Complexes. *Inorg. Chem.* **2022**, *61*, 317−327.

(24) Sarangi, R.; Cho, J.; Nam, W.; Solomon, E. I. XAS and DFT Investigation of Mononuclear Cobalt(III) Peroxo Complexes: Electronic Control of the Geometric Structure in CoO2 versus NiO2 Systems. *Inorg. Chem.* **2011**, *50*, 614−620.

(25) Tomson, N. C.; Crimmin, M. R.; Petrenko, T.; Rosebrugh, L. E.; Sproules, S.; Boyd, W. C.; Bergman, R. G.; DeBeer, S.; Toste, F. D.; Wieghardt, K. A step beyond the Feltham−Enemark notation: spectroscopic and correlated ab Initio computational support for an antiferromagnetically coupled M (II)−(NO)− description of Tp* M (NO)(M= Co, Ni). *J. Am. Chem. Soc.* **2011**, *133*, 18785.

(26) Masnovi, J.; Samsel, E. G.; Bullock, R. M. Cyclopropylbenzyl Radical Clocks. *J. Chem. Soc., Chem. Commun.* **1989**, 1044−1045.

(27) Martin, J.; Knüpfer, C.; Eyselein, J.; Färber, C.; Grams, S.; Langer, J.; Thum, K.; Wiesinger, M.; Harder, S. Highly Active Superbulky Alkaline Earth Metal Amide Catalysts for Hydrogenation of Challenging Alkenes and Aromatic Rings. *Angew. Chem., Int. Ed.* **2020**, *59*, 9102−9112.

(28) Stoll, S.; Schweiger, A. EasySpin, a comprehensive software package for spectral simulation and analysis in EPR. *J. Magn. Reson.* **2006**, *178*, 42−55.

https://doi.org/10.1021/acscatal.2c02467
ACS Catal. 2022, 12, 9933−9943